From Dots to Doughnuts: Two-Dimensionally Confined Deposition of Polyelectrolytes on Block Copolymer Templates

Meirav Oded,[†] Stephen T. Kelly,[‡,§] Mary K. Gilles,[‡] Axel H. E. Müller,[∥] and Roy Shenhar[†]*

[†] The Institute of Chemistry and the Center for Nanoscience and Nanotechnology, The Hebrew University of Jerusalem, Jerusalem 9190401, Israel.

[‡] Chemical Sciences Division, Lawrence Berkeley National Laboratory, Berkeley, California 94720, USA.

[§] Present address: Carl Zeiss X-ray Microscopy Inc., Pleasanton, CA, 94588 USA

[∥] Institute of Organic Chemistry, Johannes Gutenberg University, 55099 Mainz, Germany.

* Corresponding Author; E-mail: roys@huji.ac.il

Keywords: Block copolymers, Layer-by-Layer deposition, Patterning, Polyelectrolytes, Self-Assembly.

ABSTRACT: The combination of block copolymer templating with electrostatic self-assembly provides a simple and robust method for creating nano-patterned polyelectrolyte multilayers over large areas. Understanding the deposition of the first polyelectrolyte layer is crucial for achieving successful buildup of patterned multilayers. Here, we focus on two-dimensionally confined “dots” patterns afforded by block copolymer films featuring hexagonally-packed cylinders that are oriented normal to the substrate. Rendering the cylinder caps positively charged enables the selective deposition of negatively charged polyelectrolytes on them under salt-free conditions. The initially formed polyelectrolyte nanostructures adopt a toroidal ("doughnut") shape, which results from retraction of dangling polyelectrolyte segments into the “dots” upon drying. With increasing exposure time to the polyelectrolyte solution, the final shape of the deposited polyelectrolyte transitions from a doughnut to a hemisphere. These insights would enable the creation of patterned polyelectrolyte multilayers with increased control over adsorption selectivity of the additional incoming polyelectrolytes.

1. Introduction

Layer-by-layer (LbL) deposition has become a leading technique for creating functional coatings with controllable thickness and composition with nanometric resolution.[1, 2] This method relies on the sequential application of polyelectrolytes (PEs) with alternate charges to a charged substrate, which leads to the formation of polyelectrolyte multilayers (PEM).[3-9] The electrostatic polyelectrolyte adsorption is entropically driven due to the release of counter ions to the solution.[10] The LbL technique has been applied to various types of substrates, compositions,[11-14] and geometries[1, 15-19] using a range of PEs, including biopolymers, nanoparticles, and clays.[20-26] PEM coatings are widely applicable in medicine, sensing, molecular electronics, and surface modifications.[27-40]

Constructing PEMs on patterned substrates opens another dimension in LbL construction, which may be useful for applications that require lateral structuring or high surface area (e.g., photonics, catalysis, controlled release, and membranes). Hammond et al. studied the deposition of PEs on micron-scale patterns prepared by micro-contact printing.[41-45] These studies directly addressed the selectivity of PE adhesion to different substrates, and revealed the effects of ionic strength and PE molecular weight on the selectivity. One of the interesting observations was that high molecular weight PEs give rise to smooth deposition over the preferred stripes, while simultaneously PEs accumulated along the stripe edges. This accumulation was attributed to dangling chains of anchored PE chains that retracted from the repelling matrix.[41] Jonas et al. studied PEM construction on nano-patterned substrates prepared by electron-beam lithography.[46, 47] The main observation was that much thicker PEM deposits formed on the nano-patterned domains compared to on laterally homogeneous substrates. This behavior was attributed to the strong lateral confinement imposed by the domain dimensions.

The pioneering research described above provided important fundamental insights on confined LbL construction. However, the realization of patterned PEMs for advanced technological applications requires a simple and economic approach. Recently, we reported on sodium poly(4-styrene sulfonate) (PSS) patterning on thin films of a polystyrene-*block*-poly(2-vinylpyridine) (PS-*b*-P2VP) block copolymer (BCP) featuring a periodic pattern of positively charged stripes.[48] This study demonstrated that the deposition process is completed within a few minutes, and is followed by slower structural changes attributed to penetration of PEs and solvent molecules into the quaternized P2VP domains. Additionally, two types of PSS deposition, attributed to local variations in charge density, were observed.

In this study, we show that the utilization of films featuring hexagonally-packed dot patterns as electrostatic templates imposes two-dimensional confinement, which leads to the formation of doughnut-shaped PSS deposits. Prolonging the exposure of the substrate to the PSS solution and monitoring structural changes during "annealing", provides additional insights into the evolution of PEs that are selectively adsorbed onto periodic nanoscale patterns.

2. Materials and Methods

2.1 Materials. PS-*b*-P2VP diblock copolymer (M_n 185 kDa, PDI = 1.24, 67 wt% PS, 99 nm bulk period, denoted as $PS_{124}P2VP_{61}$) was synthesized by standard anionic polymerization using *sec*-butyllithium in tetrahydrofuran (THF) under nitrogen atmosphere. The molecular weight, size distribution and polystyrene weight fraction were all determined by gel permeation chromatography (GPC) in THF against PS standards for the PS block and comparison of the ^1H NMR signals for phenyl and pyridine groups, respectively, for the P2VP block. The periodicity of the BCP was determined by SAXS measurements. Sodium poly(4-styrenesulfonate) (PSS), M_w ~70 kDa was purchased from Sigma-Aldrich and used after soxhlet extraction for a week in ethanol. The PSS was diluted in ultrapure water (conductivity of 0.055 μ siemens cm^{-1}) to form a 0.1 M monomer concentration (20 mg mL^{-1}). 1,4-diiodobutane was purchased from Alfa-Aesar and used as received. The electrolyte solution for the reference system was prepared with tosylic acid in ultrapure water at a concentration equal to the molar equivalent of the sulfonate units of the PSS. The pH of the electrolyte solution was adjusted to the pH of the PSS solution (pH 4.7) using concentrated NaOH and HCl solutions to produce a sodium tosylate (TsONa) solution.

2.2 Sample preparation. Silicon oxide wafers were pre-cleaned in a sulfuric acid-NoChromix (purchased from Sigma-Aldrich) overnight and then rinsed with triply distilled water. $PS_{124}P2VP_{61}$ was dissolved in a 60:40 w/w mixture of THF and toluene (weight fraction of

60:40, respectively) to form a solution with a concentration of 0.8%w/w. Prior to casting the solution was filtered through a 0.22 μm PTFE syringe filter. Thin polymer films (~50 nm thickness) were obtained by spin casting the appropriate solutions at 3000 rpm for 40 s onto hydrophilic silicon oxide wafers with 3 nm-thick native oxide. The films were annealed in a closed petri dish under saturated chloroform atmosphere for different time intervals.

The dot pattern was obtained by annealing 50±1 nm-thick of cylindrical $PS_{124}P2VP_{61}$ films for 9 min. Homopolymers films of PS, P2VP and PS/P2VP blend were prepared; the blend films were obtained after 4 min annealing in chloroform. For the STXM measurements, films were initially cast on KBr pellets, floated on distilled water by dissolving the KBr substrate, and transferred onto silicon nitride membrane windows (Silson Ltd.) by slowly drawing the windows from the solution.

To prepare the ESA templates, films and vials containing 1,4-diiodobutane (DIB) were placed in a specially designed sample holder, inserted into a glass tube oven (Büchi GKR-50) and heated to 75 °C under vacuum for 42 hours.

2.3 Deposition process. The ESA templates were dipped in PSS solutions for various time intervals, dipped in ultrapure water for a few seconds, and washed with ultrapure water (for a few seconds) while spinning at 2000 rpm for 30 s. The samples were then placed under vacuum at ambient temperature for at least 24 hours prior to characterization.

2.4 Characterization. GPC measurements were performed on a Polymer Standards Service (PSS) system consisting of a PSS SDV linear M column, refractive index, and UV detectors (Thermo), multiple angle light scattering (MALS) detector (BiMwA, Brookhaven), and an online viscometer (ETA 2010, WGE Dr. Bures). Data analysis and universal calibration (with PS standards) were performed using PSS WinGPC software. High resolution scanning electron

microscopy (HR-SEM) images of the films were acquired with a Sirion microscope (FEI Company) at 3-5 kV acceleration voltage. XPS data was acquired with a Kratos Axis Ultra X-ray photoelectron spectrometer (Kratos Analytical Ltd., Manchester, UK) using an Al Ka monochromatic radiation source (1,486.7 eV) with 90° takeoff angle (i.e., analyzer is normal to sample). The high-resolution XPS spectra were collected for C 1s, I 3d, N 1s, and S 2p levels with 20 eV pass energy and 0.1 eV step. The binding energies were calibrated relative to C 1s peak energy position at 285.0 eV. Background subtraction and data analysis were performed using Casa XPS (Casa Software Ltd.) and Vision data processing program (Kratos Analytical Ltd.). All spectra where normalized to the C 1s intensity.

AFM images were acquired by a Dimension 3100 Scanning Probe Microscope (SPM) with a Nanoscope V controller, Veeco, Santa-Barbra, USA. The images were corrected by first-order flattening and processed using Nanoscope Analysis program (V1.40, Bruker). Total film thicknesses were determined by AFM profiling of a scratch made in the film using the step function. Doughnut height profiles shown in **Figure 5** were obtained by averaging 18 cross-sections for each time point after centering the dimples of all profiles. The BCP height images were analyzed using the built-in particle analysis tool. For each time point of the PSS-treated (or TsONa-treated) samples, six (four) images measuring 2×2 μm^2 were processed by the particle analysis implemented in the Nanoscope software. The depth histogram of each image (0.1 nm bin size) (see Figure S1b for a representative example) was processed by Savitzky-Golay smoothing (20 point window, second order polynomial). The histograms were fitted to three Gaussians. A threshold was set to exclude 99% of the area of the Gaussian representing the darkest pixels (corresponding to the deepest domains, i.e., the PS matrix; see Figure S1b). Figure S1c shows the qP2VP domains as turquois dots, and Figure S1d shows the corresponding

diameter histogram, showing a bimodal distribution (attributed to wide and narrow dots). Setting a threshold at the weighted average point between the two peaks of the diameter histogram enabled separate analysis for the narrow and wide dot populations (Figure S1e,f, respectively; turquois and blue dots in each image represent selected and excluded domains, respectively). After manually excluding irregularly shaped particles and particles at the boundary of the image, the average height and diameter of each population were calculated by the software (see text below Figure S1e,f).

Soft X-ray scanning transmission X-ray microscopy (STXM) is a synchrotron-based spectromicroscopy technique that images samples by raster scanning them in a focused (c.a. 30 nm) X-ray beam. The incident X-ray energy can be tuned to specific regions within the near edge X-ray absorption fine structure (NEXAFS) region to highlight particular elements or chemical functional groups. It has been used frequently to characterize atmospheric particles[49, 50] as well as polymer photoresists[51] and polymer blends,[52, 53] and technical details about STXM can be found elsewhere.[54] STXM/NEXAFS measurements were performed at beamline 11.0.2 of the Advanced Light Source at Lawrence Berkeley National Laboratory. The STXM images were processed by Fourier analysis using a high pass Gaussian filter (Figure S2).

3. Results and Discussion

Figure 1 schematically depicts our approach for assembling PSS on dot patterns featured by cylindrical PS-*b*-P2VP in thin films where the P2VP cylinders are oriented normal to the substrate. The dot pattern is obtained by spin-coating a 0.4% solution of the block copolymer in $CHCl_3$ followed by drying and brief solvent annealing in $CHCl_3$ vapor (see Experimental section). Subsequent reaction with 1,4-diiodobutane (DIB) quaternizes the pyridine rings and cross-links the P2VP domains, rendering the template amenable for electrostatic self-assembly

(ESA) (**Figure 1**b).[55-57] The reaction is performed in the gas phase to prevent structural changes to the surface pattern. In the next stage the ESA template is dipped into a PSS solution, which adsorbs on the P2VP domains (**Figure 1**c).

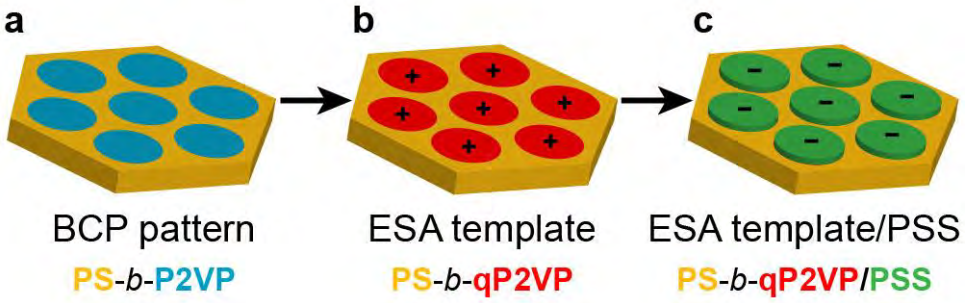

Figure 1. Schematic illustration of the approach for the formation of a dot-patterned polyelectrolyte layer using electrostatic self-assembly. Plus and minus signs in (b,c) denote the sign of the net surface charge of the domain.

3.1 Characterization of the ESA template. XPS analysis of the changes in the intensity of the nitrogen and iodine peaks after DIB treatment confirms that pyridine alkylation as well as cross-linking at the film surface has indeed occurred (Figure S3; see supporting information for additional details). From the intensities of the N and N^+ XPS signals we estimate that about 26% of the pyridine rings at the film surface have been alkylated, and the fraction of pyridine units that are cross-linked out of the total number of pyridine units in the volume sampled by the XPS is estimated to be ca. 16% (see supporting information for additional details).

Figure 2a-f show SEM and AFM images as well as cross-sectional cartoons of the dot-patterned BCP and the ESA template, prepared from a cylindrical $PS_{124}P2VP_{61}$ copolymer (subscript numbers denote M_n of the respective block in kDa; see Materials and Methods in the Experimental section). Comparing the SEM images corresponding to the dot template before and after reaction with DIB (**Figure 2**a,d respectively) shows contrast reversal. This indicates a

change in topography from P2VP depressions to protruding cylinder caps after crosslinking. This conclusion is supported by atomic force microscopy (AFM) images (**Figure 2**b,e), which show that the height contrast between the P2VP and the PS domains is reversed.

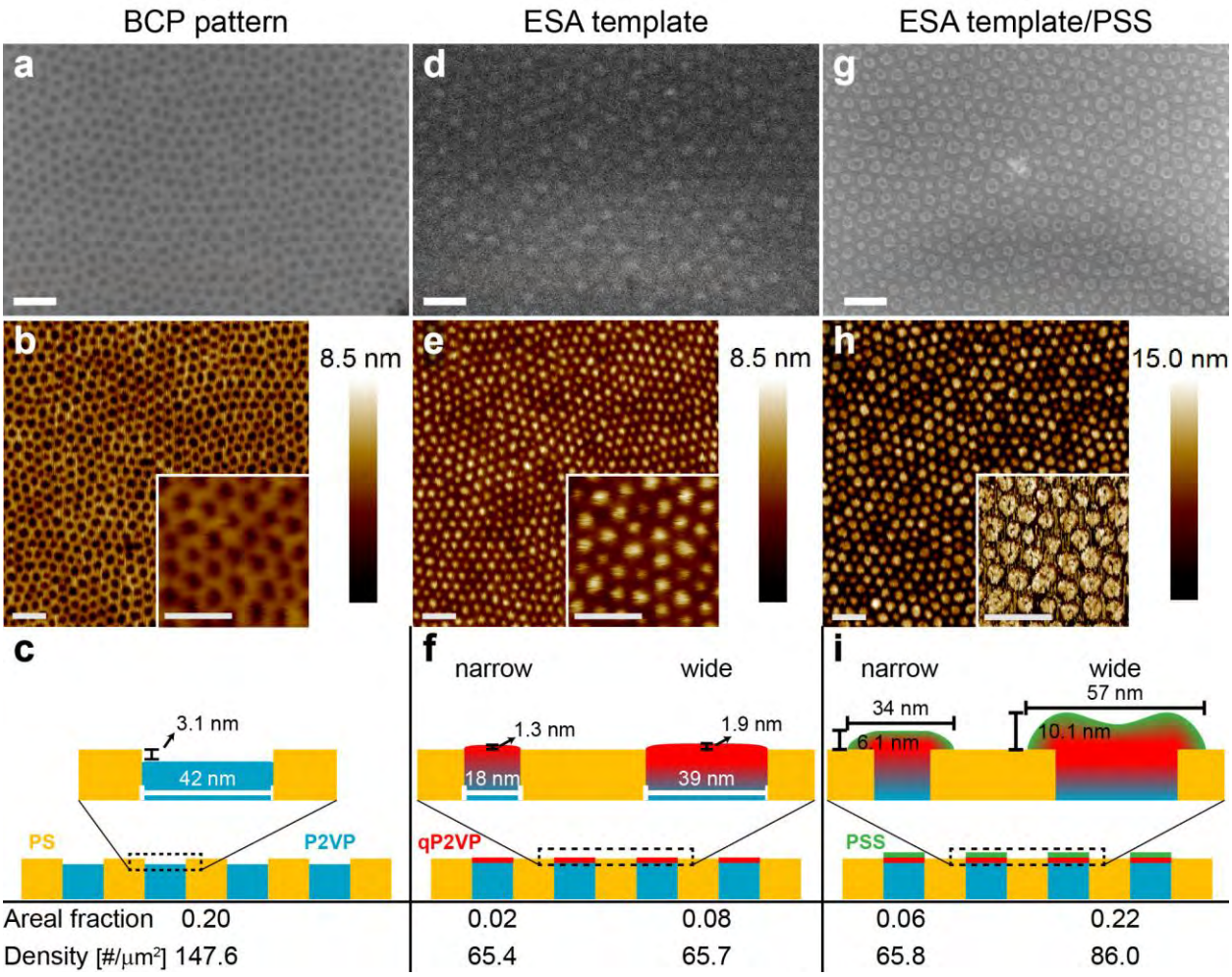

Figure 2. (a,d,g) SEM images and (b,e,h) AFM height images of $PS_{124}P2VP_{61}$ thin films after solvent annealing (BCP pattern; a,b), after reaction with DIB (ESA template; d,e), and after 30 min PSS deposition (ESA template/PSS; g,h). All scale bars correspond to 200 nm; insets in AFM images show magnified regions (b,e – height contrast; h – phase contrast, in which the dimple in the center of the cylinder is clearly visible). (c,f,i) Illustrations of the cross-sections of the top part of the P2VP cylinders at different stages of the process, showing the averaged diameters, height differences, areal fractions and number densities of cylinders. Height is enlarged by 50% compared to the width for clarity.

The transformation of the P2VP cylinders from depressions to protrusions upon DIB treatment is somewhat surprising considering that crosslinking usually shrinks the material. The changes in the volumes of the cylinders could be assessed using particle analysis, which enables quantitative determination of the average heights as well as the average diameters (see Experimental Section and Supporting Information, Figure S1 for the further details). Applying this protocol to the AFM height images of the BCP pattern reveals a mono-modal distribution of P2VP cylinder diameters centered at 42 nm. Overall, the cylinders occupy 20% of the surface area of the BCP pattern. However, crosslinking the P2VP domains leads to a clear bi-modal size distribution of the qP2VP cylinder diameters, which is also visually apparent in **Figure 2**e. This is accompanied by reduction in the surface area occupied by the cylinders to only ~10% of the surface of the ESA template. Indeed, out of the ~5,500 cylinders analyzed, about half have shrunk from 42 nm to about 39 nm, whereas the average diameter of the other half has considerably decreased to about 18 nm (**Figure 2**c,f). Nonetheless, the total number density of the cylinders has not increased.[58]

The last observation suggests that the qP2VP cylinders are crosslinked only at their top. Considering the increase in cylinder heights and the decrease in diameters and the expected shrinking in volume of the crosslinked part, we calculate that the penetration depth of the crosslinks from the original P2VP cylinder top to be at least 5 nm. The reason for the bi-modal distribution relates to inhomogeneous quaternization of the P2VP domains. Support to this assumption is found at an intermediate stage during the reaction with DIB, where the film displays both depressions and protrusions (Figure S4). This suggests that the crosslinking of a P2VP cylinder is a cooperative process, where the initial quaternization of pyridines in a domain facilitates the continuation of this process. We speculate that the transformation from depressions

to protrusions increases the exposed area of the P2VP cylinders at the surface of the film, and thus expedites the adsorption of additional DIB molecules; however, other explanations (e.g., the effect of changes in local dielectric constant) are also possible. Narrow cylinders apparently originate from P2VP domains that have started their crosslinking earlier in the process of forming the ESA template. In that sense, the wide cylinders represent an intermediate state, and feature a lower average charge density than the narrow cylinders.

3.2 Characterization of the PSS deposition process. Dipping the ESA template into the PSS solution further increases the heights and diameters of the dots while retaining the 2D pattern (**Figure 2**g-i). XPS analysis shows a prominent sulfur peak that is attributed to PSS (Figure S3c). The combination of topographical and compositional data suggests that selective deposition of PSS over the quaternized P2VP (qP2VP) domains indeed occurred. Supporting evidence for this conclusion is provided by Scanning Transmission X-ray Microscopy (STXM), which enables local elemental mapping of a scanned area with ~25 nm resolution by tuning the energy of the scanning beam to the corresponding absorption edges. Figure 3 shows an image of PS-qP2VP/PSS taken at the energy corresponding to the absorption edge of oxygen after image enhancement (see Experimental Section and Supporting Information, Figure S2 for further details). Due to enhanced absorption, the oxygen-rich PSS regions appear as round blue domains (i.e., lower intensity of transmitted photons), confirming the selectivity of the PSS adhesion to qP2VP cylinder caps. This is in agreement with insights gained from XPS analysis (see Supporting Information, Figure S3 for further details) and with the results of our previous study on PSS deposition on a striped pattern.[48]

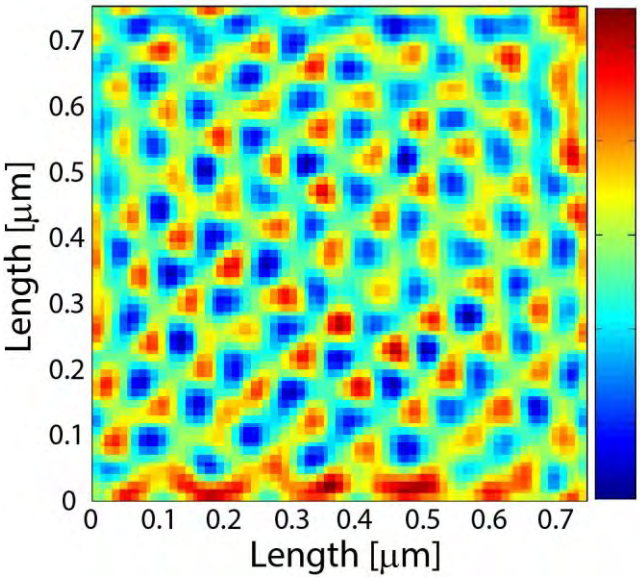

Figure 3. STXM image taken at the absorption peak in the O K edge for a $PS_{124}P2VP_{61}$ sample after PSS deposition. Blue indicates strong absorption, i.e. higher oxygen content.

A closer examination of the SEM image of the PSS-covered template (**Figure 2**g) reveals non-uniform deposition on top of each cylinder. The borders of the qP2VP/PSS domains appear to be thicker than the center of the domain (i.e., a 'doughnut' shape). The same pattern is visible in the AFM image (**Figure 2**h, particularly in the magnified phase image), which rules out the possibility that the doughnut shape is merely a beam-induced charging artefact. We speculate that the reason for this pattern arises from retraction of dangling segments of adsorbed PSS into the qP2VP domains upon solvent drying.[41]

To gain further insights on the factors governing the process of polyelectrolyte adhesion to the qP2VP domains, we monitored the evolution of PSS deposition. **Figure 4** shows representative AFM and SEM images taken at different time intervals during the course of PSS deposition, as well as quantitative analysis of the cylinder dimensions from the AFM images. In parallel, we studied the structure of ESA templates treated with sodium tosylate (TsONa) with the same monomer concentration and pH as the PSS solution (**Figure 4**i,j; empty symbols). This reference

system enables isolating the contribution of domain swelling from the structural changes imposed by the deposition of PSS.

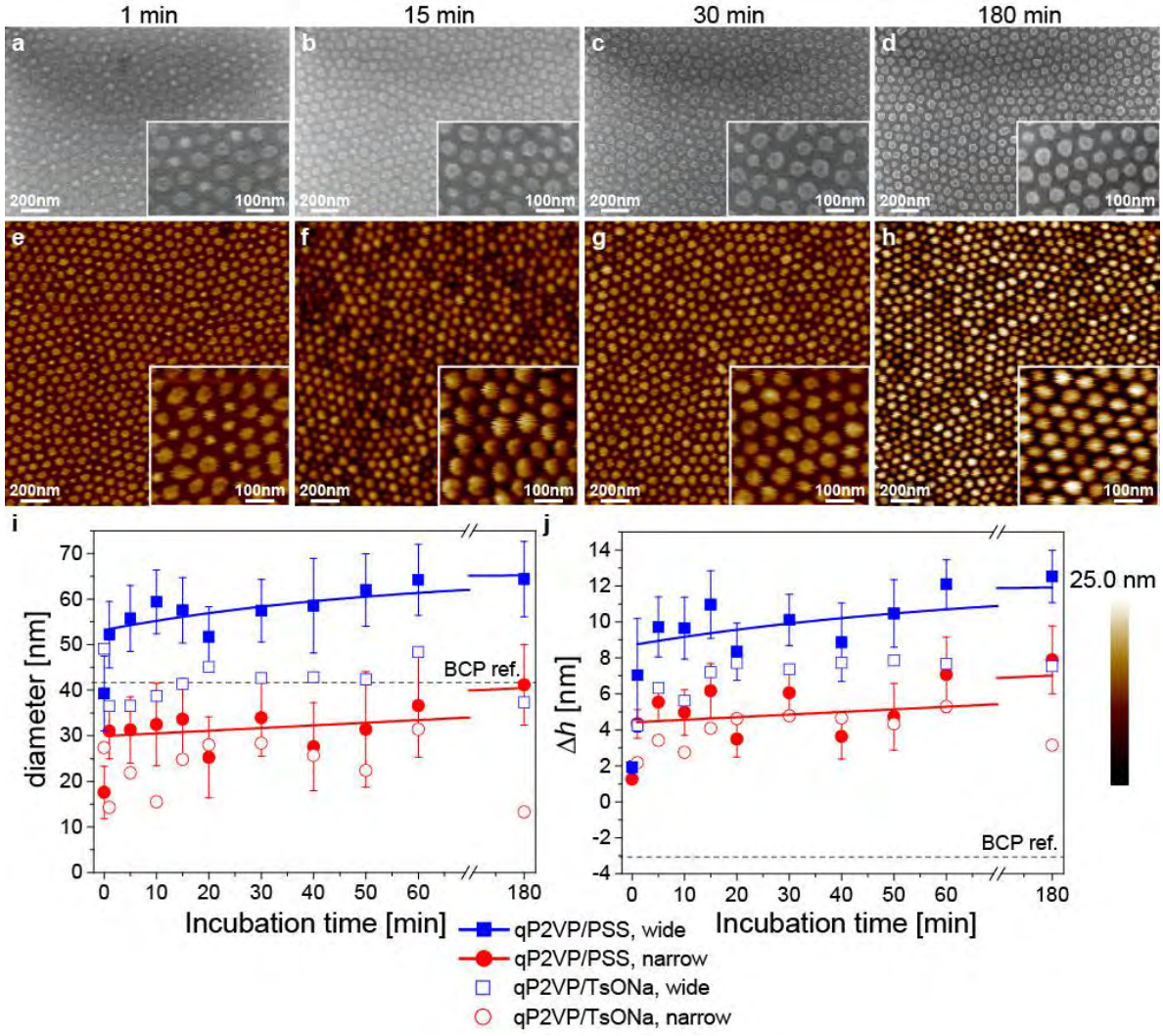

Figure 4. PSS patterning over $PS_{124}P2VP_{61}$ at different deposition times: (a-d) SEM images; (e-h) AFM images. Insets show high magnification images; height scales for AFM images are shown in the bottom right corners. (i,j) Changes in the diameter (i) and height (j) of the dots with respect to the PS matrix with deposition time (t = 0 represents the bare ESA template). Red and blue symbols correspond to the narrow and wide P2VP cylinders, respectively; empty symbols correspond to measurements performed on TsONa-treated ESA templates. Bars correspond to the standard deviation of the distribution; lines are added to guide the eye. The dashed lines represent the diameter and relative height of the cylinders in the BCP pattern for visual reference.

Exposure to the TsONa solution (control experiment) leads to a slight increase in the heights of the narrow and wide cylinders, whereas their respective diameters do not show a clear change. The adsorption of PSS leads to the following observations with respect to the narrow and wide cylinders. The behavior of the narrow cylinders is quite similar to that of the reference system both in height and diameter. The wide cylinders, however, show a marked increase in both height and diameter with increasing deposition time, which is not accounted for by the swelling of the qP2VP cylinders (as reflected by the comparison to the TsONa system). As the total number density of the dots remains the same as in the original BCP template (**Figure 2**i), we attribute the topographical changes mainly to the deposited PSS. The larger increase in the dimensions of the PSS deposited on the wide dots compared to the narrow dots suggests that the positive charge density in the wide dots is smaller, giving rise to a more coiled conformation of the deposited PSS chains.[48, 59-61] This conclusion is also corroborated by the doughnut shape of deposited PSS, which is more apparent on the wide dots.

The effect of incubation time on the shape of deposited PSS was analyzed by averaging AFM cross-sections through the centers of the wide cylinders (**Figure 5**; see the Experimental section for additional details). Upon completion of the adhesion step, after 1 min of incubation, the dimple measures 1.3 nm deep and 32 nm wide.[62] As the time of incubation in the PSS solution increases, the dimple becomes narrower and shallower. After an hour of incubation, the dimple no longer discernible by AFM (**Figure 4**h) and the deposited PSS appears spherical in shape (**Figure 5**).[63] This gradual change may be viewed as an “annealing” process, which involves structural changes that reduce the amount of dangling PSS segments (e.g., penetration of the PSS chains into the qP2VP domains). This hypothesis is supported by XPS analysis, which shows a

gradual increase in the relative amount of charged pyridines with incubation time (Figure S5d), indicating continued protonation.

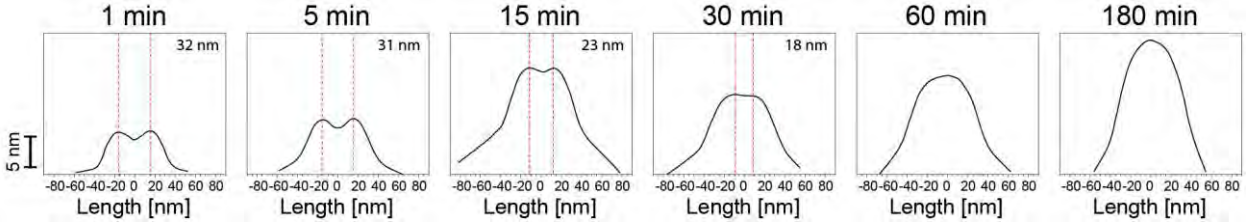

Figure 5. Averaged cross-sections through the centers of 18 wide cylinders, taken after different incubation times in PSS solution. The widths of the gaps marked by the vertical dashed lines are provided in the top right corner. Scale bar refers to the y-axis.

The negligible dependence on incubation time of the height and diameter of the narrow cylinders seen in **Figure 4**i,j (red curves) is explained by the higher charge densities that characterize these qP2VP cylinders, which lead to flatter deposition of the PSS chains. **Figure 6** illustrates our hypothesis regarding the dependence of the resulting PSS shapes on incubation time for both types of dots as a function of charge density.

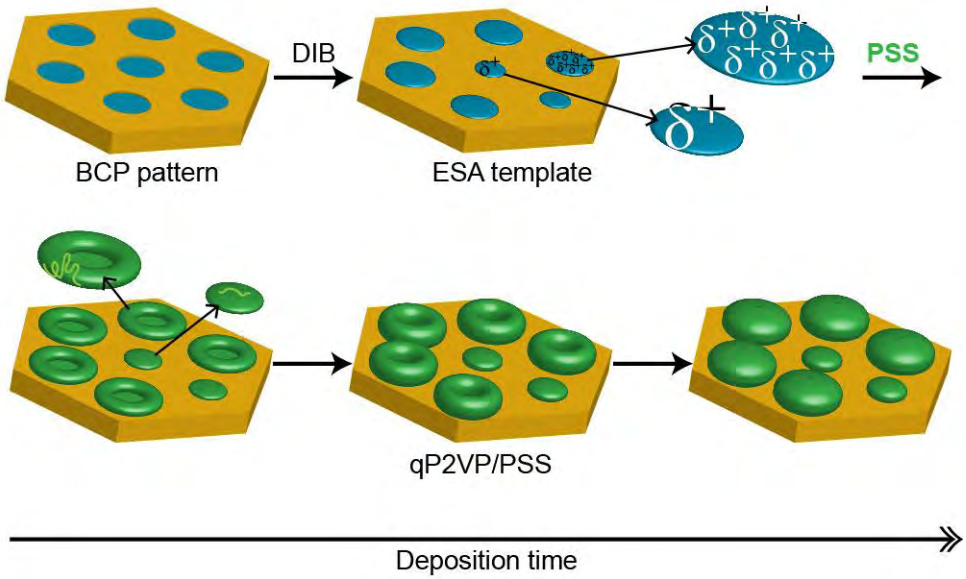

Figure 6. Illustration of the PSS structures formed on qP2VP dots after different incubation time in the PSS solution.

4. Conclusions

The two-dimensionally confined patterning of polyelectrolytes over square centimeter areas on PS-*b*-P2VP templates featuring a hexagonally-packed dot structure was studied in detail with the aim of providing a foundation for creating *patterned* polyelectrolyte multilayers. The following insights were obtained from the characterization of each step of the process. First, the quaternization/cross-linking of the P2VP domains using DIB seems to be a cooperative process, where the DIB molecules penetrate at least 5 nm into the P2VP cylinders. The reaction causes the tops of the P2VP cylinders to shrink in diameter and increase in height, transforming from depressions on the film surface to protrusions. This process yields two types of cylinders: highly cross-linked narrow cylinders, resulting from cylinders that started crosslinking early in the process, and wide cylinders featuring low charge densities. The salt-free deposition of PSS was found to be highly selective toward the quaternized P2VP domains. Statistical analysis of cylinder heights from AFM images reveals that PSS apparently deposits flatly in stretched conformations on the narrow cylinders, owing to the high density of the quaternized pyridines in these domains. Conversely, PSS deposited on the wide qP2VP cylinders in a highly coiled conformation, giving rise to a substantial increase in cylinder height above the PS matrix and the formation of a doughnut shape presumably from contraction of dangling PSS segments during drying. Extended incubation time in the PSS solution enables the PSS to reorganize on the wide qP2VP cylinders, and form more homogeneous capping of the qP2VP tops upon drying.

Based on these insights, it is anticipated that controlling the deposition time should facilitate the assembly of additional positively and negatively charged polyelectrolyte layers with retention of selectivity for a few layers. This capability will pave the way for the creation of functional

multilayers that exhibit lateral patterns with nanoscale periodicities, which would be useful for photonic and sensing applications.

Supporting Information. XPS Characterization, supplementary AFM images and analysis, STXM images and the processing procedure.

Acknowledgments. M.O. thanks the Harry and Sylvia Hoffman Leadership and Responsibility Program, and the Dalia and Dan Maydan Fellowship for financial support. The Advanced Light Source (ALS) at Lawrence Berkeley National Laboratory (LBNL) is supported by the Director, Office of Science, Office of Basic Energy Sciences, of the U.S. Department of Energy under Contract No. DE-AC02-05CH11231. M.K.G., S.T.K and Beamline 11.0.2 were supported by the same contract as well as the Condensed Phase and Interfacial Molecular Sciences Program of the U.S. Department of Energy. The authors thank Dr. Inna Popov and Dr. Vitaly Gutkin for assistance with the XHR-SEM and XPS measurements.

5. References and Comments

1. Iler RK. J. Colloid Interface Sci. 1966;21(6):569-594.
2. Decher G. Science 1997;277:1232-1237.
3. Ariga K, Hill JP, and Ji Q. Phys. Chem. Chem. Phys. 2007;9(19):2319-2340.
4. Hammond PT. AlChE J. 2011;57(11):2928-2940.
5. Li Y, Wang X, and Sun J. Chem. Soc. Rev. 2012;41(18):5998-6009.

6. Caruso F. Adv. Mater. 2001;13(1):11-22.

7. Jiang C and Tsukruk VV. Adv. Mater. 2006;18(7):829-840.

8. Bertrand P, Jonas A, Laschewsky A, and Legras R. Macromol. Rapid Commun. 2000;21:319-348.

9. Chen W and McCarthy TJ. Macromolecules 1997;30:78-86.

10. Schlenoff JB and Dubas ST. Macromolecules 2001;34(3):592-598.

11. Decher G, Hong JD, and Schmitt J. Thin Solid Films 1992;210-211(1-2):831-835.

12. Kolasinska M, Krastev R, and Warszynski P. J. Colloid Interface Sci. 2007;305(1):46-56.

13. Trubetskoy VS, Loomis A, Hagstrom JE, Budker VG, and Wolff JA. Nucleic Acids Res. 1999;27(15):3090-3095.

14. Lvov Y, Ariga K, Ichinose I, and Kunitake T. J. Am. Chem. Soc. 1995;117(22):6117-6123.

15. Decher G and Hong JD. Makromol. Chem. Macromol. Symp. 1991;46:321-327.

16. Decher G and Hong JD. Ber. Bunsen-Ges. Phys. Chem. Chem. Phys. 1991;95(11):1430-1434.

17. Wang Y, Angelatos AS, and Caruso F. Chem. Mater. 2008;20(3):848-858.

18. Caruso F, Caruso RA, and Möhwald H. Science 1998;282(5391):1111-1114.

19. Sukhorukov GB, Donath E, Davis S, Lichtenfeld H, Caruso F, Popov VI, and Mohwald H. Polym. Adv. Technol. 1998;9(10-11):759-767.

20. Kotov NA, Dekany I, and Fendler JH. J. Phys. Chem. 1995;99(35):13065-13069.

21. Lvov Y, Ariga K, and Kunitake T. Chem. Lett. 1994;23(12):2323-2326.

22. Kotov NA, Haraszti T, Turi L, Zavala G, Geer RE, Dekany I, and Fendler JH. J. Am. Chem. Soc. 1997;119(29):6821-6832.

23. Ariga K, Lvov Y, and Kunitake T. J. Am. Chem. Soc. 1997;119(9):2224-2231.

24. Lvov Y, Haas H, Decher G, Moehwald H, Mikhailov A, Mtchedlishvily B, Morgunova E, and Vainshtein B. Langmuir 1994;10(11):4232-4236.

25. Lvov Y, Ariga K, Onda M, Ichinose I, and Kunitake T. Langmuir 1997;13(23):6195-6203.

26. Shipway AN, Katz E, and Willner I. ChemPhysChem 2000;1(1):18-52.

27. Jaber JA and Schlenoff JB. Curr. Opin. Colloid Interface Sci. 2006;11(6):324-329.

28. Ho PKH, Kim JS, Burroughes JH, Becker H, Li SFY, Brown TM, Cacialli F, and Friend RH. Nature 2000;404(6777):481-484.

29. Hammond PT. Adv. Mater. 2004;16(15):1271-1293.

30. Hammond PT. Mater. Today 2012;15(5):196-206.

31. Tang ZY, Wang Y, Podsiadlo P, and Kotov NA. Adv. Mater. 2006;18(24):3203-3224.

32. Zhang X, Shi F, Niu J, Jiang YG, and Wang ZQ. J. Mater. Chem. 2008;18(6):621-633.

33. Quinn JF, Johnston APR, Such GK, Zelikin AN, and Caruso F. Chem. Soc. Rev. 2007;36(5):707-718.

34. Johnston APR, Cortez C, Angelatos AS, and Caruso F. Curr. Opin. Colloid Interface Sci. 2006;11(4):203-209.

35. Lutkenhaus JL and Hammond PT. Soft Matter 2007;3(7):804-816.

36. Siqueira Jr JR, Caseli L, Crespilho FN, Zucolotto V, and Oliveira Jr ON. Biosens. Bioelectron. 2010;25(6):1254-1263.

37. Iost RM and Crespilho FN. Biosens. Bioelectron. 2012;31(1):1-10.

38. Delcea M, Möhwald H, and Skirtach AG. Adv. Drug Delivery Rev. 2011;63(9):730-747.

39. Jewell CM and Lynn DM. Adv. Drug Delivery Rev. 2008;60(9):979-999.

40. Oliveira MB and Mano JF. Biotechnol. Progr. 2011;27(4):897-912.

41. Hammond PT and Whitesides GM. Macromolecules 1995;28(22):7569-7571.

42. Clark SL, Montague MF, and Hammond PT. Supramol. Sci. 1997;4(1-2):141-146.

43. Clark SL, Montague MF, and Hammond PT. Macromolecules 1997;30(23):7237-7244.

44. Clark SL and hammond PT. Adv. Mater. 1998;10(18):1515-1519.

45. Clark SL and Hammond PT. Langmuir 2000;16(26):10206-10214.

46. Pallandre A, Glinel K, Jonas AM, and Nysten B. Nano Lett. 2004;4(2):365-371.

47. Pallandre A, Moussa A, Nysten B, and Jonas AM. Adv. Mater. 2006;18(4):481-486.

48. Oded M, Kelly ST, Gilles MK, Müller AHE, and Shenhar R. Soft Matter 2016, in press (DOI: 10.1039/C6SM00381H).

49. Moffet RC, Rodel TC, Kelly ST, Yu XY, Carroll GT, Fast J, Zaveri RA, Laskin A, and Gilles MK. Atmos. Chem. Phys. 2013;13(20):10445-10459.

50. Moffet RC, Tivanski AV, and Gilles MK. Scanning Transmission X-ray Microscopy Applications in Atmospheric Aerosol Research. In: Signorell R and Reid JP, editors. Fundamentals and Applications in Aerosol Spectroscopy. Boca Raton, Fl: CRC Press, Taylor & Francis Group, 2011. pp. 434-436.

51. Muntean L, Planques R, Kilcoyne ALD, Leone SR, Gilles MK, and Hinsberg WD. J. Vac. Sci. Technol., B 2005;23(4):1630-1636.

52. Smith AP, Laurer JH, Ade HW, Smith SD, Ashraf A, and Spontak RJ. Macromolecules 1997;30(3):663-666.

53. Morin C, Ikeura-Sekiguchi H, Tyliszczak T, Cornelius R, Brash JL, Hitchcock AP, Scholl A, Nolting F, Appel G, Winesett DA, Kaznacheyev K, and Ade H. J. Electron. Spectrosc. Relat. Phenom. 2001;121(1-3):203-224.

54. Kilcoyne ALD, Tyliszczak T, Steele WF, Fakra S, Hitchcock P, Franck K, Anderson E, Harteneck B, Rightor EG, Mitchell GE, Hitchcock AP, Yang L, Warwick T, and Ade H. J. Synchrotron Radiat. 2003;10:125-136.

55. Shenhar R and Ben-Lulu M "Selective layer-by-layer deposition over block copolymer domains", US patent application, PCT/IL2012/050206, WO 2012/172554 A2, Filing date 13 June, Priority Data: 61/496,128 13 June 2011.

56. Lee W, Lee SY, Briber RM, and Rabin O. Adv. Funct. Mater. 2011;21(18):3424-3429.

57. Liu Z, Chang T, Huang H, and He T. RSC Advances 2013;3(43):20464-20470.

58. The slight decrease (11%) in the total number density of the cylinders in the ESA template compared to the BCP pattern is attributed to an underestimation of the number of the narrow cylinders caused by the thresholding procedure.

59. Ladam G, Schaad P, Voegel JC, Schaaf P, Decher G, and Cuisinier F. Langmuir 2000;16(3):1249-1255.

60. McAloney RA, Sinyor M, Dudnik V, and Goh MC. Langmuir 2001;17(21):6655-6663.

61. Dubas ST and Schlenoff JB. Macromolecules 1999;32(24):8153-8160.

62. The value of the dimple depth represents a lower bound of the actual depth considering convolution effects caused by the AFM tip curvature.

63. The doughnut shape is still visible in the SEM images after 180 min of incubation. However, as the SEM contrast is influenced not only by height differences but also by variations in electron density, we prefer to rely on the AFM data for the topographical analysis.

Table of Contents Graphic

From Dots to Doughnuts: Two-Dimensionally Confined Deposition of Polyelectrolytes on Block Copolymer Templates

Meirav Oded, Stephen T. Kelly, Mary K. Gilles, Axel H. E. Müller, and Roy Shenhar*

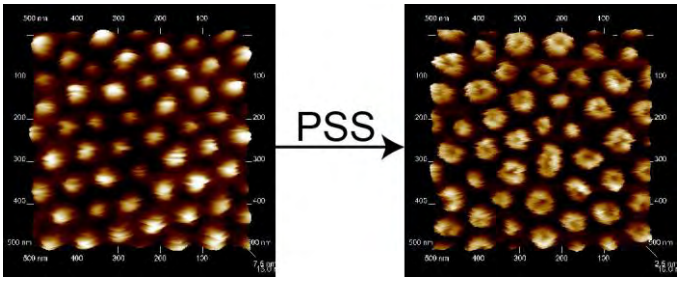

Supplementary Material (online publication)

Click here to download Supplementary Material (online publication): #17 dots paper - SI.pdf